Research Article

Nano Research
2024, 17(8): 7020–7026

ISSN 1998-0124 CN 11-5974/O4
https://doi.org/10.1007/s12274-024-6732-0

Overcoming side reaction effects in the colloidal synthesis of ZnSe/ZnS core/shell quantum dots with an etching strategy

Jinhua He[1], Chenhui Wang[2] (✉), Mingrui Liu[1], Muhammad Ramzan[1], Zhiwei Long[1], Xian-gang Wu[1], Yu Chen[1], and Haizheng Zhong[1] (✉)

[1] *MIIT Key Laboratory for Low-Dimensional Quantum Structure and Devices, School of Materials Science and Engineering, Beijing Institute of Technology, Beijing 100081, China*
[2] *Beijing Engineering Research Center for Mixed Reality and Advanced Display Technology, School of Optics and Photonics, Beijing Institute of Technology, Beijing 100081, China*

Received: 26 March 2024 / **Revised:** 24 April 2024 / **Accepted:** 28 April 2024

ABSTRACT

The potential use of large-size ZnSe quantum dots as blue emitters for display applications has greatly inspired the colloidal synthesis. Herein, we report the negative effects of side reactions of large-size ZnSe quantum dots. The side reactions between oleic acid and oleylamine generated amidation products and H_2O, which led to the hydrolysis of $Zn(OA)_2$ to $Zn(OH)_2$ and the subsequent formation of zinc oxide (ZnO) and zinc bis[diphenylphosphinate] ($Zn(DPPA)_2$) precipitates. These side reactions resulted in the formation of a defective surface including a Se-rich surface and oxygen-related defects. Such negative effects can be overcome by adopting an etching strategy using potassium fluoride and myristic acid in combination. By overcoating a ZnS shell, blue emissive ZnSe/ZnS quantum dots with a maximum photoluminescence quantum yield of up to 91% were obtained. We further fabricated ZnSe quantum dots-based blue light-emitting diodes with an emission peak at 456 nm. The device showed a turn-on voltage of 2.7 V with a maximum external quantum efficiency of 4.2% and a maximum luminance of 1223 $cd \cdot m^{-2}$.

KEYWORDS

quantum dots, ZnSe, side reactions, surface etching, light-emitting diodes

1 Introduction

Quantum dot light-emitting diodes (QLEDs) are emerging as promising next-generation display technology due to their super high brightness, wide color gamut, and facile solution process ability [1–8]. In comparison with the well-developed Cd-based QLEDs, the performance of Cd-free QLEDs still lags behind, in particular for the blue emissive electroluminescence (EL) devices [9–13]. Very recently, ZnSe quantum dots (QDs) attracted a great of attention as blue emitters for QLED display applications including ZnSeTe QDs [14–21] and large-size ZnSe QDs [22, 23]. Among the challenges in the colloidal synthesis of these Cd-free QDs, the broadened emission of ZnSeTe QDs and low photoluminescence quantum yield (PLQY) of large-size ZnSe QDs are obstacles to fabricating high-performance blue QLEDs [23, 24]. For large-size ZnSe QDs, the formation of interfacial defects hindered the fabrication of ZnSe/ZnS core/shell QDs with pure-blue color (455–475 nm) and high PLQY [23, 25, 26].

Previous works have demonstrated that the surface defects of InP QDs are correlated with two side reactions involving carboxylic acids. Basically, one involves the reaction between free carboxylic acids and phosphonide [27], and the other involves the formation of a hydroxylated surface, which is related to the H_2O generated from the ketonization reaction of free carboxylic acids [28]. Such defects can be alleviated by employing an etching treatment with hydrofluoric acid (HF) or zinc fluoride (ZnF_2) [29–31]. Recently, HF etching strategy has been successfully adapted for the synthesis of ZnSeTe QDs [16, 32]. However, for large-size ZnSe QDs, the underlying formation mechanisms of surface defects remain unclear [22, 23].

In this work, we investigated the side reactions occurring during the synthesis of large-size ZnSe QDs. We observed the turbidity of the colloidal solution and the PL decrease of ZnSe cores, which are related to the side reactions between oleic acid (OA) and oleylamine (OLA). The precipitates from the turbid solution were characterized using X-ray diffraction (XRD) measurement, suggesting the formation of zinc oxide (ZnO) and zinc bis[diphenylphosphinate] ($Zn(DPPA)_2$). The negative effects of these side reactions on the surface of large-size ZnSe cores are clarified with the X-ray photoelectron spectroscopy (XPS) and Fourier transform infrared (FT-IR) spectroscopy measurements. These negative effects can be overcome by using a modified etching strategy with potassium fluoride (KF) and myristic acid (MA) in combination, resulting in large-size ZnSe/ZnS core/shell QDs with a maximum PLQY of over 90%. Based on the above results, we proposed a surface evolution mechanism to explain the etching process during the synthesis of ZnSe cores. With these high-quality blue emissive QDs, we further fabricated a QLED device with pure-blue light at 456 nm.

2 Results and discussion

A modified reactivity-controlled epitaxial growth (RCEG) strategy was employed for the colloidal synthesis of large-size ZnSe QDs

Address correspondence to Chenhui Wang, chwang@bit.edu.cn; Haizheng Zhong, hzzhong@bit.edu.cn

[22]. Figure 1(a) shows photos of the reaction solutions at four different stages, including the preparation of Zn precursor A (Stage 1), the formation of small-size ZnSe cores (Stage 2), the growth of large-size ZnSe cores without (Stage 3) and with etching agents (Stage 4). At Stage 1, Zn precursor A with OA to OLA ratio of 0.2 was prepared at 120 °C (see Section 4.3 for details). At Stage 2, small-size ZnSe cores were obtained by injecting highly reactive Se-DPP precursor into Zn precursor A at 280 °C and reacting for 30 min. At Stage 3, large-size ZnSe cores were achieved by alternately injecting Zn precursor B with OA to OLA ratio of 1 and Se-trioctylphosphine (Se-TOP) precursors at 300 °C (see Section 4.3 for details). Without using OLA, the solution of large-size ZnSe cores is maintained in a clear state during the colloidal synthesis. With using OLA, the solution of large-size ZnSe cores became turbid at Stage 3 (Fig. S1 in the Electronic Supplementary Material (ESM)), indicating the existence of side reactions. At Stage 3, the PLQY of large-size ZnSe QDs first increases to 60% with the red shift of the PL emission and then experiences a sudden decrease after the PL emission exceeds 450 nm (Fig. 1(b)). At Stage 4, the use of KF and MA in combination can overcome the turbidity of ZnSe cores with PL emission at 450 nm (labeled as ZnSe-450), resulting in an enhanced PLQY of up to 73% (Fig. 1(c)).

As indicated in the XRD patterns (Fig. 2(a)), the white precipitates purified from the turbid solution at Stage 3 are mainly composed of $Zn(DPPA)_2$ and ZnO. The formation of $DPPA^-$ may be related to the multi-step oxidation of DPP in the precursor solution with intermediate products including diphenylphosphine oxide (DPPO) and DPPA. Because the amidation reaction between OA and OLA can generate H_2O, which may be related to the formation of ZnO. To understand the amidation reaction, we monitored the reactions between OA and OLA at different temperatures by applying ^1H nuclear magnetic resonance (^1H NMR) measurements. As shown in Fig. 2(b), the ^1H signal at 11.2 ppm, which represents the carboxyl group of OA, disappears when OA and OLA are mixed at 120 °C. Simultaneously, a proton amine signal ($-NH_3^+$) appears at 6.2 ppm, indicating proton transfer between OA and OLA [33]. When the temperature rose above 200 °C, an amidation reaction occurred between the carboxyl group of OA and the amino group of OLA [34]. This is evidenced by the disappearance of the ^1H signal of $-NH_3^+$ and the down-field shift in the ^1H signals of α-CH_2 and β-CH_2 groups from OLA [35]. As the temperature increased, the mixed OA and OLA solutions changed from light yellow to dark brown and eventually turned into gel with the temperature decrease (Fig. S2 in the ESM). This further confirms the formation of amidation products at high temperatures. Figure 2(c) illustrates the side reactions occurring during the synthesis of large-size ZnSe QDs at Stage 3. The amidation reaction between OA and OLA leads to the formation of H_2O, which results in the hydrolysis of $Zn(OA)_2$ into $Zn(OH)_2$ and its subsequent decomposition into ZnO precipitate. Therefore, we deduced that $Zn(DPPA)_2$ formed from the reaction between $Zn(OH)_2$ and DPPA.

To gain more insights into the sudden decrease in PLQY observed when the PL peak redshifts over 450 nm at Stage 3 (Fig. 1(b)), XPS measurements were conducted on ZnSe cores with PL emissions at 432 and 450 nm (labeled as ZnSe-432 and ZnSe-450, respectively). As shown in Fig. S3 in the ESM, the O 1s signal can be curve-fitted as two peaks with binding energies of about 531.6 and 532.5 eV. The higher energy peak is assigned to oxygen-related defects (surface oxidation and hydroxyl adsorption), and the lower energy peak is associated with oxygen-related surface ligands, including OA, oleate (OA^-), and TOP oxide (TOPO). For ZnSe-432, a single O 1s peak at a binding energy of 531.6 eV is observed, indicating the coordination of oxygen-related surface ligands. For ZnSe-450, the O 1s peak of oxygen-related surface ligands significantly decreases, while another peak with a relative area ratio of 87% appears at a higher binding energy of 532.5 eV (Table S1 in the ESM), suggesting the existence of oxygen-related defects on the ZnSe surface [25, 36, 37]. The appearance of oxygen-related defects results from the side reactions occurring on the surface of large-size ZnSe cores.

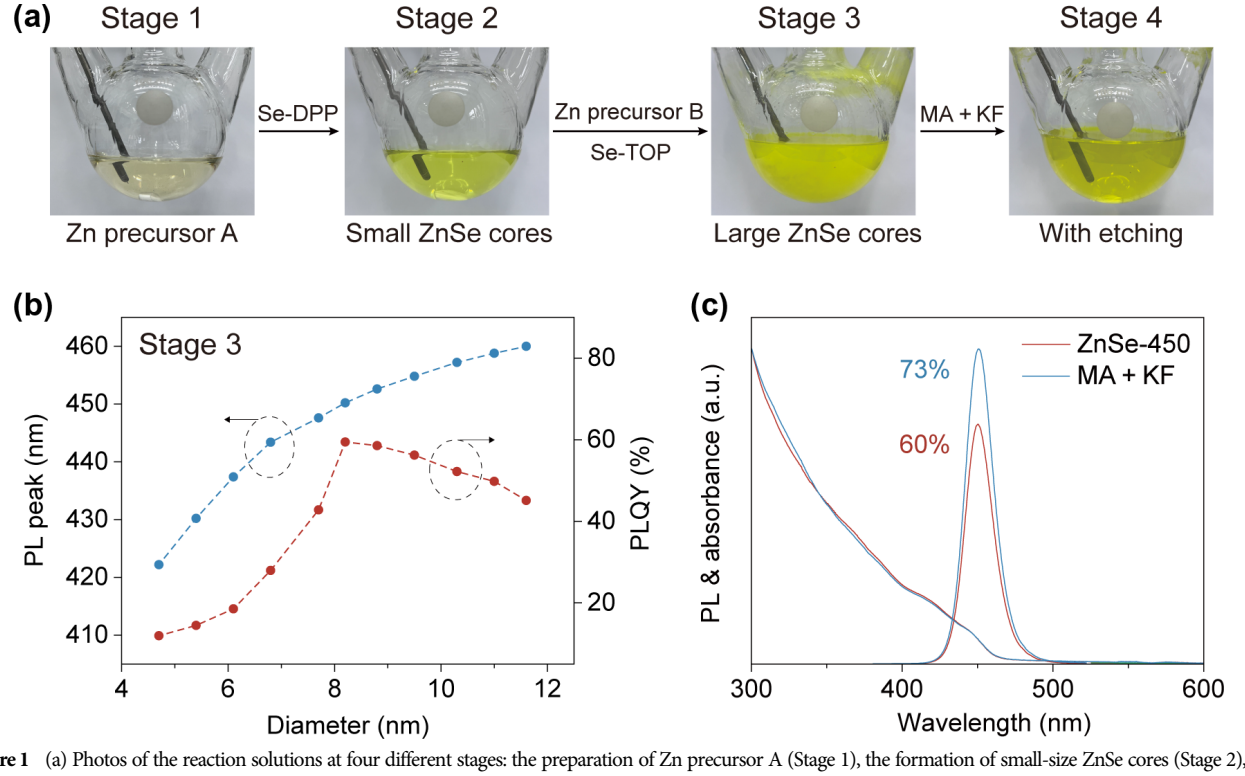

Figure 1 (a) Photos of the reaction solutions at four different stages: the preparation of Zn precursor A (Stage 1), the formation of small-size ZnSe cores (Stage 2), the growth of large-size ZnSe cores without (Stage 3) and with etching agents (Stage 4). The ratio of OA to OLA in Zn precursor A and Zn precursor B is 0.2 and 1, respectively. (b) Evolution of PL peak and PLQY with increasing diameter of ZnSe QDs at Stage 3. (c) PL and UV–vis absorption spectra of ZnSe-450 and etched ZnSe-450 using KF and MA in combination.

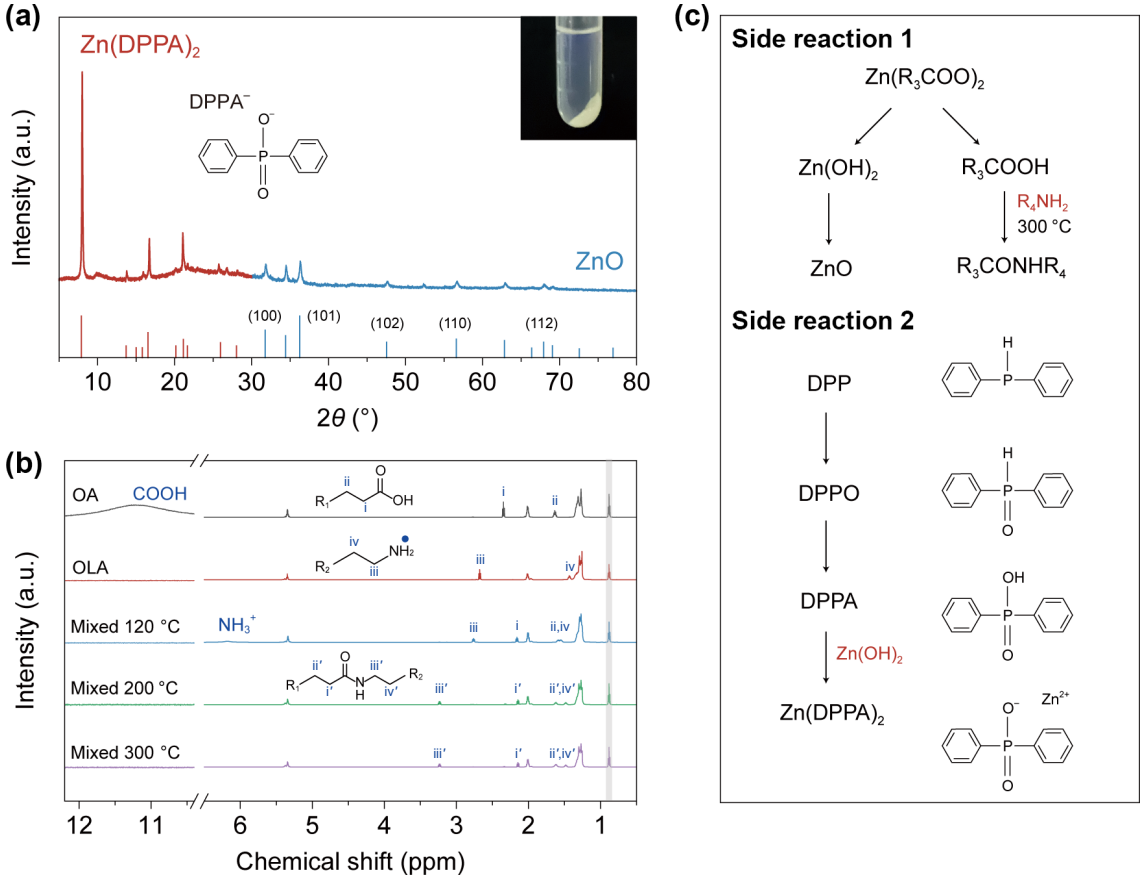

Figure 2 (a) XRD patterns of the purified precipitates obtained from the solution of large-size ZnSe cores at Stage 3. The JPCDS No. is 19-1705 and 79-0206 for $Zn(DPPA)_2$ and ZnO, respectively. JPCDS: Joint Committee on Powder Diffraction Standards. Inset, a photo of the precipitates. (b) ^{1}H NMR spectra (chloroform-d^1, 600 MHz) of OA, OLA, and a mixture of OA and OLA at different temperatures. R_1: $C_8H_{17}(CH)_2C_5H_{10}$; R_2: $C_8H_{17}(CH)_2C_6H_{12}$; R_3: $C_8H_{17}(CH)_2C_7H_{14}$; R_4: $C_8H_{17}(CH)_2C_8H_{16}$. (c) Illustration of the side reactions.

Furthermore, we noticed that ZnSe-450 exhibits a Se-rich surface with a Zn to Se atomic ratio of 0.57 (Fig. S4 in the ESM), which typically results in the formation of mid-gap states and the PL quenching [38, 39]. The increase of PLQY of ZnSe-450 at Stage 4 can be associated with the effective etching of the defective surface by the use of KF and MA in combination.

To explore the etching effects of ZnSe-450 at Stage 4, we investigated the etching process with the use of KF and MA either alone or in combination. As shown in Fig. 3(a), the use of KF or/and MA weakens the stretching vibrations of N–H in the range of 3240–3400 cm^{-1} and the bending vibrations of N–H in the range of 1620–1675 cm^{-1} [40], while using MA leads to an enhanced asymmetric stretching vibration signal of carboxylate (COO^-) in the range of 1515–1570 cm^{-1} [41, 42]. These results suggest that weakly coordinated OLA ligands can be partially detached by fluoride ions (F^-) or/and COO^-, and the carboxylic acids significantly contribute to the coordination of carboxylate ligands with ZnSe-450. Moreover, the use of KF and MA in combination significantly improves the solubility of ZnSe-450 (Fig. 1(a), Fig. S5 in the ESM) and increases the surface Zn to Se atomic ratio from 0.57 to 1.08 (Fig. S4 in the ESM), suggesting the strong coordination ability of $Zn(R_3COO)_2$ and R_3COO^- ligands.

Figure 3(b) and Table S1 in the ESM reveal that the use of KF or MA alone results in a decrease in the relative area ratio of the O 1s peak at 532.5 eV from 87% to 43% and 55%, respectively. In comparison, a significant reduction of the ratio to 6% is observed when using KF and MA in combination, indicating the positive effects of KF and MA on alleviating oxygen-related surface defects. As demonstrated in Fig. 3(c), the use of KF alone leads to a decrease in PLQY from 60% to 55% and the average lifetime from 53.7 to 44.4 ns, as well as an increase in the proportion of short-lifetime components associated with non-radiative recombination (Table S2 in the ESM). The use of MA alone slightly affects the PL properties of ZnSe-450. The use of KF and MA in combination significantly enhances the PLQY from 60% to 73% and the average lifetime from 53.7 to 76.1 ns, along with a larger proportion of long-lifetime components. Therefore, the use of KF and MA in combination improves the PL properties of ZnSe-450, which can be explained by the alleviation of the defective surface with a Se-rich surface and oxygen-related defects.

Figure 3(d) schematically illustrates the surface evolution of large-size ZnSe QDs at different stages. The surface of small-size ZnSe cores is covered by OA and OLA ligands simultaneously. By injecting Zn precursor B with OA to OLA ratio of 1 at Stage 3, the side reactions between OA and OLA exacerbate, leading to the formation of ZnO and $Zn(DPPA)_2$ precipitates. The side reactions occurring on the surface induce the evolution into a defective surface with a Se-rich surface and oxygen-related defects. After etching using KF and MA in combination at Stage 4, the precipitates are eliminated and the defective surface is alleviated. Herein, we further discussed the effects of MA and KF with the consideration of the side reactions. In principle, MA can react with ZnO and $Zn(DPPA)_2$ precipitates to provide $Zn(R_3COO)_2$ and R_3COO^- ligands for the Se-rich surface. In addition, it can also react with excess OLA to suppress the amidation reaction. On the other hand, KF may promote amine ligand exchange and alleviate oxygen-related defects by combining with carboxylic acids. Notably, the participation of MA may enhance the etching effect of F^- by providing H protons [29–31]. As shown in Fig. S6 in the ESM, this modified etching strategy significantly improves the PLQY of ZnSe-450 than the sample fabricated with HF etching. Unlike the reported passivation mechanism involving hydrogen halides [16], the F 1s XPS spectrum indicates the etched ZnSe-450

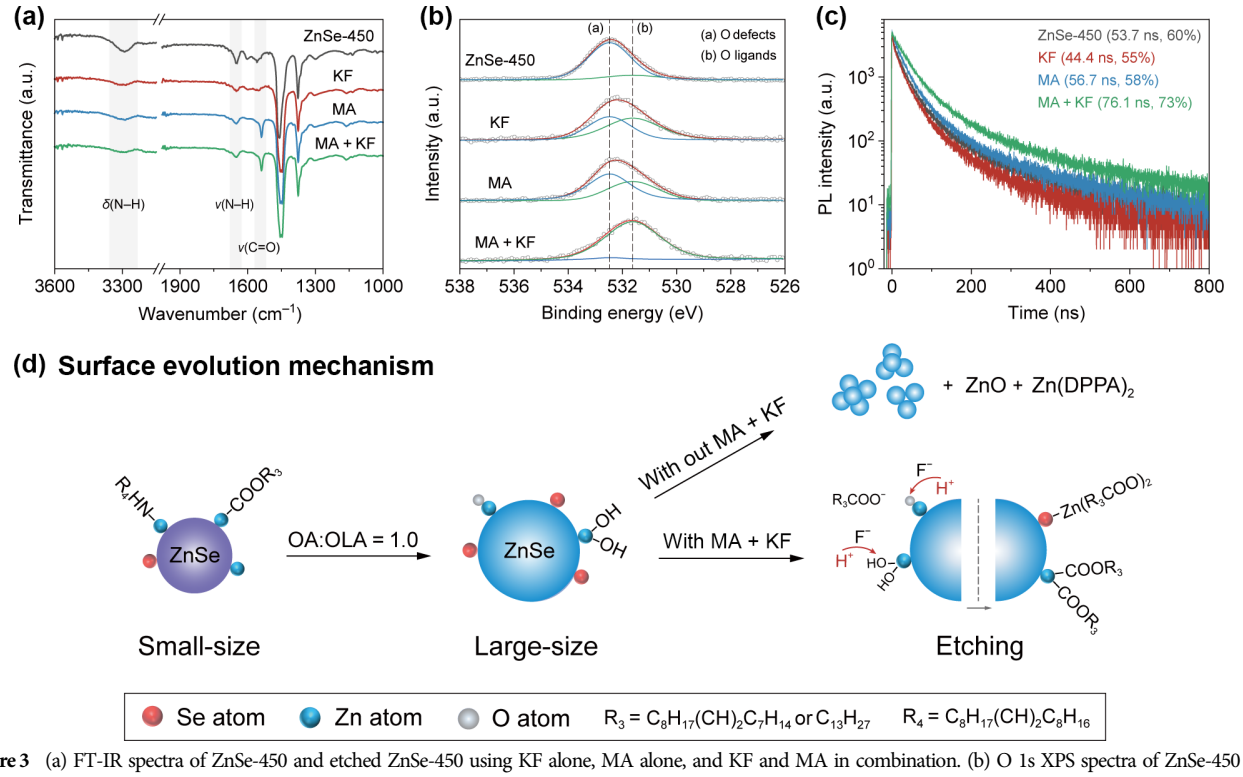

Figure 3 (a) FT-IR spectra of ZnSe-450 and etched ZnSe-450 using KF alone, MA alone, and KF and MA in combination. (b) O 1s XPS spectra of ZnSe-450 and etched ZnSe-450 using KF alone, MA alone, and KF and MA in combination. (c) TRPL spectra of ZnSe-450 and etched ZnSe-450 using KF alone, MA alone, and KF and MA in combination. (d) Schematic illustration of surface evolution mechanism at different stages.

does not have F^- on the surface (Fig. S7 in the ESM).

We further explored the etching strategy of other combinations with different organic acids and metal fluoride (Fig. 4). The combination of KF and organic carboxylic acids, including caprylic acid (CA), stearic acid (SA), behenic acid (BA), octacosanoic acid (OCA), OA, 10-undecenoic acid (10-UDA), and erucic acid (EA) all contribute to the enhancement of PLQY of large-size ZnSe cores. However, the use of inorganic acids such as phosphoric acid (PA) leads to PL quenching. In addition, the combination of MA and metal fluorides, including zinc fluoride (ZnF_2), magnesium fluoride (MgF_2), nickel fluoride (NiF_2), and sodium fluoride (NaF), also exhibit positive effects on the PL properties of ZnSe-450. The above results prove that our etching strategy is universal for improving the PLQY of large-size ZnSe QDs.

By using KF and MA in combination, we obtained etched ZnSe-450 with PLQY increased to 73% (Fig. 5(a)). After overcoating the ZnS shell with another etching process, the etched ZnSe/ZnS core/shell QDs exhibit a further enhanced PLQY of 91% compared with 76% of those without etching (Fig. S8 in the ESM). As shown in Fig. S9 and Table S3 in the ESM, the average lifetime of etched ZnSe/ZnS QDs is shorter than those without etching, which can be explained by a reduction in the proportion of long-lifetime components associated with non-radiative recombination. XRD results confirm the zinc blende structure of the etched ZnSe-450 and etched ZnSe/ZnS core/shell QDs (Fig. 5(b)). Transmission electron microscopy (TEM) images show the etched

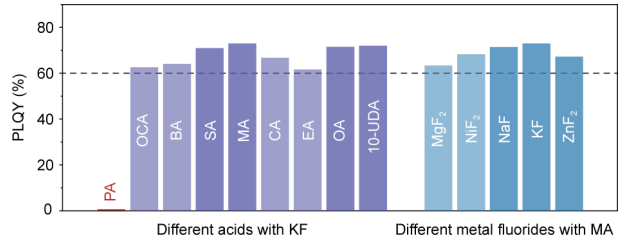

Figure 4 PLQYs of the etched ZnSe-450 by the use of long-chain organic carboxylic acids and metal fluorides in combination.

ZnSe-450 and etched ZnSe/ZnS QDs have an average size of 8.9 and 10.8 nm, respectively (Figs. 5(c) and 5(d), and Fig. S10 in the ESM). The structure, morphology and size distribution statistics of ZnSe-450 and ZnSe/ZnS QDs without etching are shown in Figs. S11 and S12 in the ESM.

Furthermore, we fabricated QLEDs with a device structure of indium tin oxide (ITO)/poly(3,4-ethylenedioxythiophene): poly (styrenesulfonate) (PEDOT:PSS)/poly((9,9-dioctylfluorenyl-2,7-diyl)-co-(4,4'-(*N*-(4-*sec*-butylphenyl)diphenylamine)) (TFB)/ etched QDs/$Zn_{0.9}Mg_{0.1}O$/aluminum (Al) (Fig. 6(a)). The energy-band levels of ZnSe/ZnS QDs were determined by applying ultraviolet photoelectron spectroscopy (UPS) measurement (Fig. S13 in the ESM). The EL spectra under various forward biases peaks at 456 nm with a full width half maximum (FWHM) of 22 nm (Fig. 6(b)), corresponding to the Commission Internationale de l'Eclairage (CIE) color coordinates of (0.18, 0.08). The current density–luminance–voltage (*J*–*L*–*V*) and external quantum efficiency (EQE)–luminance curves of the devices are shown in Figs. 6(c) and 6(d). The device exhibits sub-bandgap turn-on characteristics (< 2.7 V) (Fig. 6(c)), indicating efficient electron and hole injection. A maximum luminance of 1223 cd·m^{-2} is achieved at 6.9 V (Fig. 6(c)) and a maximum EQE of 4.2% is achieved at 4.5 V with a luminance of 345 cd·m^{-2} (Fig. 6(d)). Figure S14 in the ESM shows the histogram of the maximum EQE for twenty etched QDs-based QLEDs. As shown in Table S4 in the ESM, this is the first report of QLEDs based on large-size ZnSe/ZnS QDs emitting in the pure-blue region (455–475 nm), showing their potential use in the high-color-purity display application.

3 Conclusion

In summary, we demonstrated the side reactions during the synthesis of large-size ZnSe QDs including the amidation reaction between OA and OLA, the formation of ZnO precipitate from the hydrolysis of $Zn(OA)_2$ with an intermediate of $Zn(OH)_2$, the formation of $Zn(DPPA)_2$ precipitate from the reaction between $Zn(OH)_2$ and DPPA. We discussed the negative effects of these

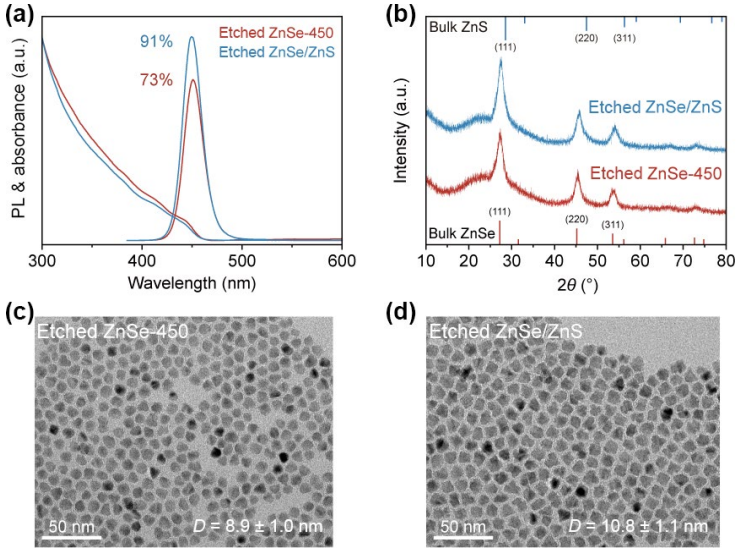

Figure 5 (a) PL and UV–vis absorption spectra with corresponding PLQYs of etched ZnSe-450 using KF and MA in combination, and the etched ZnSe/ZnS QDs. (b) XRD patterns of etched ZnSe-450 using KF and MA in combination, and etched ZnSe/ZnS QDs. JCPDS No. 88-2345 and 77-2100 for bulk ZnSe and bulk ZnS, respectively. ((c) and (d)) TEM images of etched ZnSe-450 and etched ZnSe/ZnS QDs.

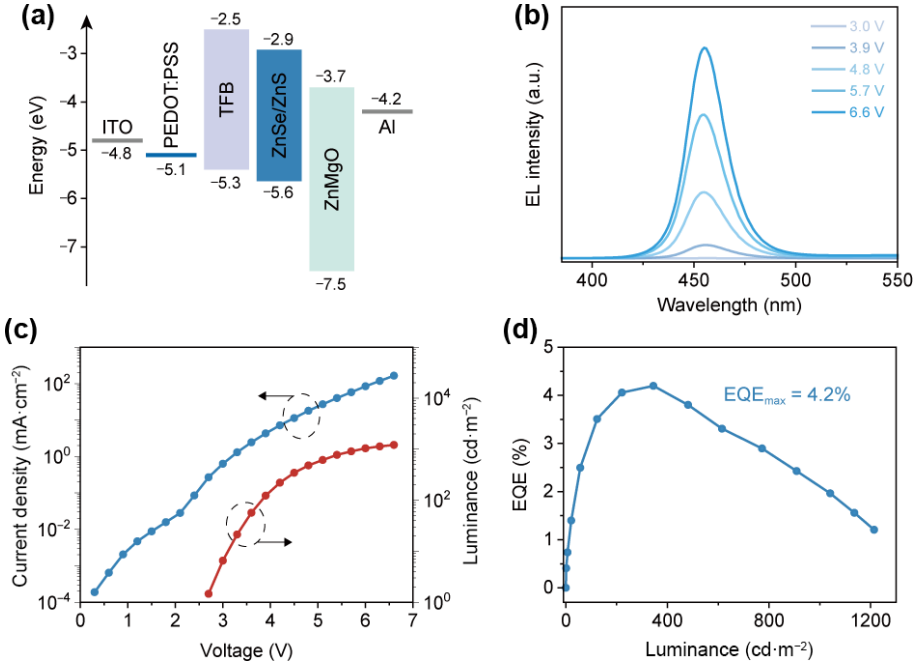

Figure 6 (a) Energy-band level diagram of the QLED. (b) Voltage-dependent EL spectra of the QLED. (c) Current density–luminance–voltage characteristic of the QLED. (d) EQE–luminance characteristic of the QLED.

side reactions on the formation of Se-rich surface and oxygen-related defects. These negative effects can be overcome with a modified etching strategy that uses organic acid and metal fluoride in combination, leading to the synthesis of high-quality ZnSe/ZnS core/shell QDs with PLQY up to 91%. In addition, the large-size ZnSe QDs-based QLEDs in the pure-blue emission region (455–475 nm) were achieved with a maximum EQE of 4.2% and a maximum luminance of 1223 cd·m^{-2}. As we know, this is the first report of ZnSe QDs-based QLED with a pure-blue color for display application. We believe that our understanding of side reactions in colloidal synthesis will promote the fabrication of high-quality materials for optoelectronic applications.

4 Experimental

4.1 Chemicals

$ZnAc_2$ (99.99%), Se (99.99%), S (99.998%), OA (90%), OLA (70%), 1-octadecene (ODE, 90%), TOP (97%), zinc acetate dihydrate ($ZnAc_2{\cdot}2H_2O$, 99.999%), magnesium acetate tetrahydrate ($MgAc_2{\cdot}4H_2O$, 99.98%), tetramethylammonium hydroxide pentahydrate (TMAH·$5H_2O$, 97%), dimethyl sulfoxide (DMSO, 99.9%), ethanol (99.5%), chlorobenzene (99.8%), and deuterated chloroform (chloroform-d^1) were purchased from Sigma-Aldrich. DPP (95%), MA (99%), caprylic acid (99%), stearic acid (98%), behenic acid (85%), octacosanoic acid (98%), 10-undecenoic acid (98%), erucic acid (99%), phosphoric acid (99%), KF (99.9%), ZnF_2 (99.99%), MgF_2 (99.99%), NiF_2 (97%), and NaF (99.99%) were purchased from Aladdin. PEDOT:PSS was purchased from Xi'an Polymer Light Technology Corp. TFB was purchased from American Dye Source.

4.2 Preparation of precursor solutions

The synthesis of ZnSe/ZnS core/shell QDs was conducted using four precursor solutions. Se-DPP precursor was prepared in a nitrogen-filled glove box by dissolving 0.4 mmol Se in 1 mL DPP. Zn precursor B was prepared in a three-neck flask by dissolving

16 mmol $Zn(Ac)_2$ in 5 mL OA, 5 mL OLA and 30 mL ODE and degassed at 120 °C under vacuum for 1 h and kept at 80 °C under argon for further use. Se-TOP was prepared in a three-neck flask by dissolving 20 mmol Se in 10 mL TOP. S-TOP was prepared in a three-neck flask by dissolving 20 mmol S in 10 mL TOP. Both Se-TOP and S-TOP precursors were degassed at 120 °C under vacuum for 30 min and reacted at 150 °C under argon for 1 h, then kept at room temperature for further use.

4.3 Synthesis of ZnSe/ZnS core/shell QDs

Zn precursor A was prepared in a three-neck flask by dissolving 0.4 mmol $Zn(Ac)_2$ in 0.2 mL OA, 1 mL OLA, and 10 mL ODE and degassed at 120 °C under vacuum for 1 h, followed by heating at 280 °C. Then, 0.5 mL Se-DPP was injected into the flask, followed by raising the temperature to 300 °C and reacting for 30 min. For the epitaxial growth of ZnSe core, 5 mL Zn precursor B and 0.5 mL Se-TOP were injected alternatively at a rate of 2 mL·h^{-1}. For the growth of ZnS shell, 3 mL Zn precursor B and 0.3 mL S-TOP were injected alternatively at a rate of 1 mL·h^{-1}. The solution was then cooled to room temperature, followed by purification with ethanol and hexane.

4.4 Etching treatment

Solution for etching treatment was prepared in a nitrogen-filled glove box by dissolving 0.3 mmol KF and 3 mmol MA in 1 mL ODE. The mixture was dissolved and kept at 60 °C for use. The preparation of the solution using other organic carboxylic acids and metal fluorides instead of KF and MA followed the same method. For the etching treatment of ZnSe and ZnSe/ZnS QDs, the solution was injected quickly into the flask and reacted for 30 min.

4.5 Synthesis of $Zn_{0.9}Mg_{0.1}O$ QDs

Colloidal $Zn_{0.9}Mg_{0.1}O$ QDs were synthesized by dropping an ethanol solution (10 mL) of TMAH·5H_2O (5 mmol) into a DMSO solution (30 mL) of $ZnAc_2$·2H_2O (2.7 mmol) and $MgAc_2$·4H_2O (0.3 mmol), followed by stirring for 1 h. Then the QDs were purified from the solution with ethyl acetate and dispersed in ethanol.

4.6 Device fabrication

The patterned ITO substrates were sequentially cleaned with deionized water, acetone, ethanol, and isopropanol in an ultrasonic bath. The dried substrates were treated under oxygen plasma etching for 3 min. PEDOT:PSS was first spin-coated onto the substrates at 4000 rpm for 40 s and baked at 150 °C for 20 min in air, then the samples were transferred into a nitrogen-filled glove box (O_2 ≤ 1 ppm, H_2O ≤ 1 ppm). TFB (in chlorobenzene, 8 mg·mL^{-1}) was spin-coated at 2000 rpm for 40 s and baked at 150 °C for 30 min. Blue ZnSe/ZnS QDs (in octane, 20 mg·mL^{-1}) were spin-coated at 2000 rpm for 40 s. $Zn_{0.9}Mg_{0.1}O$ QDs (30 mg·mL^{-1}) were spin-coated at 3000 rpm for 40 s and baked at 80 °C for 20 min. Finally, Al (100 nm) was deposited by thermal evaporation under a high vacuum of 10^{-4} Pa. The devices were encapsulated in a glove box by using an acid-free ultraviolet-curable resin, followed by annealing at 80 °C for 30 min. The active area of the device was 4 mm^2.

4.7 Measurements

Steady-state PL spectra were recorded on a Tianjin Gangdong F-380 fluorescence spectrometer (excitation: 365 nm). Steady-state ultraviolet–visible (UV–vis) absorption spectra were recorded on a Mapada UV-6100 UV–vis spectrophotometer. The PLQYs of the QDs were tested by using a Hamamatsu C9920-02 absolute PLQY measurement system composed of a PMA-12 photonic multichannel analyzer and an integrating sphere (excitation: 365 nm). ^{1}H NMR spectra were recorded on a 600-MHz Bruker AVANCE III spectrometer. XRD patterns were recorded on a Bruker D8 Advance X-ray diffractometer with a Cu Kα radiation source (λ = 1.5406 Å). TEM images were recorded on a FEI Tecnai G2 F30 transmission electron microscopy. Time-resolved PL (TRPL) spectra were recorded on a Horiba Scientific DeltaFlex TCSPC lifetime fluorometer (excitation: 365 nm). FT-IR spectra were recorded on a Thermo Scientific Nicolet iS50 FT-IR spectrometer with an attenuated total reflectance (ATR) mode. XPS and UPS spectra were recorded on a Thermo Scientific Escalab 250Xi spectrometer. A monochromatic Al Kα radiation source ($h\nu$ = 1,486.6 eV) was used for XPS, and a He I radiation source ($h\nu$ = 21.2 eV) was used for UPS. QLEDs were characterized at room temperature in a nitrogen-filled glovebox by using a Keithley 2400 source meter and a SpectraScan PR-788 spectroradiometer. The EQEs of the devices were calculated with the assumption of Lambertian emission pattern, according to the previously reported method [43].

Acknowledgements

This work was by supported by the National Natural Science Foundation of China (No. U23A20683) and the Beijing Natural Science Foundation (No. Z210018).

Electronic Supplementary Material: Supplementary material (digital photos of the reaction solutions, PL and absorption spectra, PL and FWHM evolution, PLQY data, size distribution statistics from TEM images, XPS spectra, and UPS spectra) is available in the online version of this article at https://doi.org/10.1007/s12274-024-6732-0.

References

[1] Shirasaki, Y.; Supran, G. J.; Bawendi, M. G.; Bulović, V. Emergence of colloidal quantum-dot light-emitting technologies. *Nat. Photonics* **2013**, *7*, 13–23.

[2] De Arquer, F. P. G.; Talapin, D. V.; Klimov, V. I.; Arakawa, Y.; Bayer, M.; Sargent, E. H. Semiconductor quantum dots: Technological progress and future challenges. *Science* **2021**, *373*, eaaz8541.

[3] Jang, E.; Jang, H. Review: Quantum dot light-emitting diodes. *Chem. Rev.* **2023**, *123*, 4663–4692.

[4] Kim, J.; Roh, J.; Park, M.; Lee, C. Recent advances and challenges of colloidal quantum dot light-emitting diodes for display applications. *Adv. Mater.*, in press, DOI: 10.1002/adma.202212220.

[5] Dai, X. L.; Zhang, Z. X.; Jin, Y. Z.; Niu, Y.; Cao, H. J.; Liang, X. Y.; Chen, L. W.; Wang, J. P.; Peng, X. G. Solution-processed, high-performance light-emitting diodes based on quantum dots. *Nature* **2014**, *515*, 96–99.

[6] Deng, Y. Z.; Peng, F.; Lu, Y.; Zhu, X. T.; Jin, W. X.; Qiu, J.; Dong, J. W.; Hao, Y. L.; Di, D. W.; Gao, Y. et al. Solution-processed green and blue quantum-dot light-emitting diodes with eliminated charge leakage. *Nat. Photonics* **2022**, *16*, 505–511.

[7] Chen, X. T.; Lin, X. F.; Zhou, L. K.; Sun, X. J.; Li, R.; Chen, M. Y.; Yang, Y. X.; Hou, W. J.; Wu, L. J.; Cao, W. R. et al. Blue light-emitting diodes based on colloidal quantum dots with reduced surface-bulk coupling. *Nat. Commun.* **2023**, *14*, 284.

[8] Gao, Y.; Li, B.; Liu, X. N.; Shen, H. B.; Song, Y.; Song, J. J.; Yan, Z. J.; Yan, X. H.; Chong, Y. H.; Yao, R. Y. et al. Minimizing heat generation in quantum dot light-emitting diodes by increasing quasi-Fermi-level splitting. *Nat. Nanotechnol.* **2023**, *18*, 1168–1174.

[9] Deng, X. Z.; Zhang, F. J.; Zhang, Y.; Shen, H. B. Heavy-metal-free blue-emitting ZnSe(Te) quantum dots: Synthesis and light-emitting applications. *J. Mater. Chem. C* **2023**, *11*, 14495–14514.

[10] Won, Y. H.; Cho, O.; Kim, T.; Chung, D. Y.; Kim, T.; Chung, H.; Jang, H.; Lee, J.; Kim, D.; Jang, E. Highly efficient and stable

InP/ZnSe/ZnS quantum dot light-emitting diodes. *Nature* **2019**, *575*, 634–638.
[11] Chao, W. C.; Chiang, T. H.; Liu, Y. C.; Huang, Z. X.; Liao, C. C.; Chu, C. H.; Wang, C. H.; Tseng, H. W.; Hung, W. Y.; Chou, P. T. High efficiency green InP quantum dot light-emitting diodes by balancing electron and hole mobility. *Commun. Mater.* **2021**, *2*, 96.
[12] Kim, K. H.; Jo, J. H.; Jo, D. Y.; Han, C. Y.; Yoon, S. Y.; Kim, Y.; Kim, Y. H.; Ko, Y. H.; Kim, S. W.; Lee, C. et al. Cation-exchange-derived InGaP alloy quantum dots toward blue emissivity. *Chem. Mater.* **2020**, *32*, 3537–3544.
[13] Zhang, W. D.; Tan, Y. Z.; Duan, X. J.; Zhao, F. Q.; Liu, H. C.; Chen, W.; Liu, P.; Liu, X. G.; Wang, K.; Zhang, Z. K. et al. High quantum yield blue InP/ZnS/ZnS quantum dots based on bromine passivation for efficient blue light-emitting diodes. *Adv. Opt. Mater.* **2022**, *10*, 2200685.
[14] Jang, E. P.; Han, C. Y.; Lim, S. W.; Jo, J. H.; Jo, D. Y.; Lee, S. H.; Yoon, S. Y.; Yang, H. Synthesis of alloyed ZnSeTe quantum dots as bright, color-pure blue emitters. *ACS Appl. Mater. Interfaces* **2019**, *11*, 46062–46069.
[15] Han, C. Y.; Lee, S. H.; Song, S. W.; Yoon, S. Y.; Jo, J. H.; Jo, D. Y.; Kim, H. M.; Lee, B. J.; Kim, H. S.; Yang, H. More than 9% efficient ZnSeTe quantum dot-based blue electroluminescent devices. *ACS Energy Lett.* **2020**, *5*, 1568–1576.
[16] Kim, T.; Kim, K. H.; Kim, S.; Choi, S. M.; Jang, H.; Seo, H. K.; Lee, H.; Chung, D. Y.; Jang, E. Efficient and stable blue quantum dot light-emitting diode. *Nature* **2020**, *586*, 385–389.
[17] Bi, Y. H.; Cao, S.; Yu, P.; Du, Z. T.; Wang, Y. J.; Zheng, J. J.; Zou, B. S.; Zhao, J. L. Reducing emission linewidth of pure-blue ZnSeTe quantum dots through shell engineering toward high color purity light-emitting diodes. *Small* **2023**, *19*, 2303247.
[18] Cheng, C. Y.; Yu, B. B.; Huang, F.; Gao, L.; Cao, K. Q.; Zang, P. P.; Zheng, K. B.; Tian, J. J. Near-unity quantum yield ZnSeTe quantum dots enabled by controlling shell growth for efficient deep-blue light-emitting diodes. *Adv. Funct. Mater.*, in press, DOI: 10.1002/adfm.202313811.
[19] Kim, Y. H.; Yoon, S. Y.; Yang, H. Blue-emissive ZnSeTe quantum dots and their electroluminescent devices. *J. Phys. Chem. Lett.* **2024**, *15*, 2142–2151.
[20] Yuan, C. X.; Tian, F. S.; Chen, S. M. ZnSeTe blue top-emitting QLEDs with color saturation near Rec.2020 standards and efficiency over 18.16%. *Nano Res.* **2023**, *16*, 5517–5524.
[21] Cho, O.; Park, S.; Chang, H.; Kim, J.; Kim, J.; Kim, S.; Kim, T.; Kwak, J. Investigation of operation and degradation mechanisms in ZnTeSe blue quantum-dot light-emitting diodes by identifying recombination zone. *Nano Res.* **2024**, *17*, 6527–6533.
[22] Long, Z. W.; Liu, M. R.; Wu, X. G.; Gu, K.; Yang, G. L.; Chen, Z.; Liu, Y.; Liu, R. H.; Zhong, H. Z. A reactivity-controlled epitaxial growth strategy for synthesizing large nanocrystals. *Nat. Synth.* **2023**, *2*, 296–304.
[23] Long, Z. W.; Yang, G. L.; Shao, R. W.; Chen, Z.; Liu, Y.; Liu, R. H.; Zhong, H. Z. The strain effects and interfacial defects of large ZnSe/ZnS core/shell nanocrystals. *Small* **2024**, *20*, 2306602.
[24] Lee, S. H.; Song, S. W.; Yoon, S. Y.; Jo, D. Y.; Kim, S. K.; Kim, H. M.; Kim, Y.; Park, S. M.; Yang, H. Heterostructural tailoring of blue ZnSeTe quantum dots toward high-color purity and high-efficiency electroluminescence. *Chem. Eng. J.* **2022**, *429*, 132464.
[25] Min, J. J.; Zhang, Y.; Zhou, Y. M.; Xu, D. D.; Garoufalis, C. S.; Zeng, Z. P.; Shen, H. B.; Baskoutas, S.; Jia, Y.; Du, Z. L. Size engineering of trap effects in oxidized and hydroxylated ZnSe quantum dots. *Nano Lett.* **2022**, *22*, 3604–3611.
[26] Zhang, J. K.; Li, J. Z.; Ye, Z. K.; Cui, J. T.; Peng, X. G. Hot-electron-induced photochemical properties of CdSe/ZnSe core/shell quantum dots under an ambient environment. *J. Am. Chem. Soc.* **2023**, *145*, 13938–13949.
[27] Choi, Y.; Hahm, D.; Bae, W. K.; Lim, J. Heteroepitaxial chemistry of zinc chalcogenides on InP nanocrystals for defect-free interfaces with atomic uniformity. *Nat. Commun.* **2023**, *14*, 43.
[28] Cros-Gagneux, A.; Delpech, F.; Nayral, C.; Cornejo, A.; Coppel, Y.; Chaudret, B. Surface chemistry of InP quantum dots: A comprehensive study. *J. Am. Chem. Soc.* **2010**, *132*, 18147–18157.
[29] Talapin, D. V.; Gaponik, N.; Borchert, H.; Rogach, A. L.; Haase, M.; Weller, H. Etching of colloidal InP nanocrystals with fluorides: Photochemical nature of the process resulting in high photoluminescence efficiency. *J. Phys. Chem. B* **2002**, *106*, 12659–12663.
[30] Kim, T. G.; Zherebetskyy, D.; Bekenstein, Y.; Oh, M. H.; Wang, L. W.; Jang, E.; Alivisatos, A. P. Trap passivation in indium-based quantum dots through surface fluorination: Mechanism and applications. *ACS Nano* **2018**, *12*, 11529–11540.
[31] Li, H. Y.; Zhang, W. J.; Bian, Y. Y.; Ahn, T. K.; Shen, H. B.; Ji, B. T. ZnF_2-assisted synthesis of highly luminescent InP/ZnSe/ZnS quantum dots for efficient and stable electroluminescence. *Nano Lett.* **2022**, *22*, 4067–4073.
[32] Lee, Y. J.; Kim, S.; Lee, J.; Cho, E.; Won, Y. H.; Kim, T.; Kim, D. Crystallographic and photophysical analysis on facet-controlled defect-free blue-emitting quantum dots. *Adv. Mater.* **2024**, *36*, 2311719.
[33] De Roo, J.; Ibáñez, M.; Geiregat, P.; Nedelcu, G.; Walravens, W.; Maes, J.; Martins, J. C.; Van Driessche, I.; Kovalenko, M. V.; Hens, Z. Highly dynamic ligand binding and light absorption coefficient of cesium lead bromide perovskite nanocrystals. *ACS Nano* **2016**, *10*, 2071–2081.
[34] Rowell, J. L.; Jia, Y. F.; Shi, Z. X.; Molina Villarino, A.; Kang, M.; Yoon, D.; Jiang, K. Z.; Abruña, H. D.; Muller, D. A.; Robinson, R. D. General route to colloidally stable, low-dispersity manganese-based ternary spinel oxide nanocrystals. *J. Am. Chem. Soc.* **2023**, *145*, 17406–17419.
[35] Lanigan, R. M.; Sheppard, T. D. Recent developments in amide synthesis: Direct amidation of carboxylic acids and transamidation reactions. *Eur. J. Org. Chem.* **2013**, *2013*, 7453–7465.
[36] Dupin, J. C.; Gonbeau, D.; Vinatier, P.; Levasseur, A. Systematic XPS studies of metal oxides, hydroxides and peroxides. *Phys. Chem. Chem. Phys.* **2000**, *2*, 1319–1324.
[37] Valtiner, M.; Borodinb, S.; Grundmeier, G. Preparation and characterisation of hydroxide stabilised ZnO(0001)–Zn–OH surfaces. *Phys. Chem. Chem. Phys.* **2007**, *9*, 2406–2412.
[38] Lin, S. X.; Li, J. Z.; Pu, C. D.; Lei, H. R.; Zhu, M. Y.; Qin, H. Y.; Peng, X. G. Surface and intrinsic contributions to extinction properties of ZnSe quantum dots. *Nano Res.* **2020**, *13*, 824–831.
[39] Gao, Y.; Peng, X. G. Photogenerated excitons in plain core CdSe nanocrystals with unity radiative decay in single channel: The effects of surface and ligands. *J. Am. Chem. Soc.* **2015**, *137*, 4230–4235.
[40] Dai, M. Q.; Yung, L. Y. L. Ethylenediamine-assisted ligand exchange and phase transfer of oleophilic quantum dots: Stripping of original ligands and preservation of photoluminescence. *Chem. Mater.* **2013**, *25*, 2193–2201.
[41] Anderson, N. C.; Hendricks, M. P.; Choi, J. J.; Owen, J. S. Ligand exchange and the stoichiometry of metal chalcogenide nanocrystals: Spectroscopic observation of facile metal-carboxylate displacement and binding. *J. Am. Chem. Soc.* **2013**, *135*, 18536–18548.
[42] Zhang, J.; Zhang, H. B.; Cao, W. C.; Pang, Z. F.; Li, J. Z.; Shu, Y. F.; Zhu, C. Q.; Kong, X. Q.; Wang, L. J.; Peng, X. G. Identification of facet-dependent coordination structures of carboxylate ligands on CdSe nanocrystals. *J. Am. Chem. Soc.* **2019**, *141*, 15675–15683.
[43] Jin, W. X.; Deng, Y. Z.; Guo, B. B.; Lian, Y. X.; Zhao, B. D.; Di, D. W.; Sun, X. W.; Wang, K.; Chen, S. M.; Yang, Y. X. et al. On the accurate characterization of quantum-dot light-emitting diodes for display applications. *npj Flex. Electron.* **2022**, *6*, 35.